



**HAL**  
open science

## **Pd and Pd@PdO core–shell nanoparticles supported on Vulcan carbon XC-72R: comparison of electroactivity for methanol electro-oxidation reaction**

L. P. A. Guerrero-Ortega, E. Ramirez-Meneses, R. Cabrera-Sierra, L. Palacios-Romero, Karine Philippot, C. Santiago-Ramírez, L. Lartundo-Rojas, A. Manzo-Robledo

### ► To cite this version:

L. P. A. Guerrero-Ortega, E. Ramirez-Meneses, R. Cabrera-Sierra, L. Palacios-Romero, Karine Philippot, et al.. Pd and Pd@PdO core–shell nanoparticles supported on Vulcan carbon XC-72R: comparison of electroactivity for methanol electro-oxidation reaction. *Journal of Materials Science*, 2019, 54 (21), pp.13694-13714. <10.1007/s10853-019-03843-8>. <hal-02388801>

**HAL Id: hal-02388801**

**<https://hal.science/hal-02388801v1>**

Submitted on 9 Dec 2020

HAL is a multi-disciplinary open access archive for the deposit and dissemination of scientific research documents, whether they are published or not. The documents may come from teaching and research institutions in France or abroad, or from public or private research centers.

L'archive ouverte pluridisciplinaire HAL, est destinée au dépôt et à la diffusion de documents scientifiques de niveau recherche, publiés ou non, émanant des établissements d'enseignement et de recherche français ou étrangers, des laboratoires publics ou privés.



HAL Authorization

Pd and Pd@PdO core-shell nanoparticles supported on Vulcan carbon XC-72R: comparison of electroactivity for methanol electro-oxidation reaction

L.P.A. Guerrero-Ortega<sup>a</sup>, E. Ramírez-Meneses<sup>b\*</sup>, R. Cabrera-Sierra<sup>a</sup>, L.M. Palacios-Romero<sup>b</sup>, K. Philippot<sup>c</sup>, C.R. Santiago-Ramírez<sup>a</sup>, L. Lartundo-Rojas<sup>d</sup>, A. Manzo-Robledo<sup>a\*\*</sup>

<sup>a</sup> Instituto Politécnico Nacional. Laboratorio de Electroquímica y Corrosión, Escuela Superior de Ingeniería Química e Industrias Extractivas-IPN UPALM, C. P. 07738, México.

<sup>b</sup> Departamento de Ingeniería Química, Industrial y de Alimentos, Universidad Iberoamericana, Prolongación Paseo de la Reforma 880, Lomas de Santa Fe. C.P. 01219, Ciudad de México, México.

<sup>c</sup> CNRS, LCC (Laboratoire de Chimie de Coordination), CNRS. 205 Route de Narbonne, BP 44099, F-31077 Toulouse Cedex 4, France; Université de Toulouse, UPS, INPT, F-31077 Toulouse Cedex 4, France.

<sup>d</sup> Centro de Nanociencias y Micro Nanotecnologías, Instituto Politécnico Nacional, UPALM, C. P. 07738, México.

\*e-mail: esther.ramirez@ibero.mx

\*\*e-mail: amanzor@ipn.mx

## Abstract

A Nanomaterial based on Pd-nanoparticles supported onto Vulcan carbon (XC-72R) were prepared by the organometallic approach in one-pot and mild conditions (3 bar hydrogen and room temperature) using Pd(dba)<sub>2</sub> (bis (dibenzylideneacetone) palladium (0)) as metal source and hexadecylamine (HDA) as stabilizer. High resolution transmission electron microscopy (HR-TEM) evidenced the presence of well-dispersed Pd-nanoparticles of ca. 4.5 nm mean size onto the carbon support (Pd/HDA/C). Scanning and transmission electron microscopy with electron energy loss spectroscopy, STEM-EELS allowed to determine the chemical composition of the nanomaterials. When the Pd/HDA/C nanomaterial was submitted to heating-treatment (ht) at 400 °C under air (referred as Pd/HDA/C@air-ht), X-ray photoelectron spectroscopy (XPS) and HR-TEM/STEM-EELS analyses suggested the presence of interactions between PdO and Pd(0) as a result of the formation of Pd@PdO core-shell nanoparticles. The highest oxidation current magnitude during methanol oxidation reaction (MOR) is ascribed to the heat-treated material, linked with a better electron and mass transfer processes at the electrode interface. This can be attributed to electronic interactions at the core-shell formed, that might promote different redox processes at the electrode interface during CH<sub>3</sub>OH-deprotonation in the alkaline electrolyte.

Keywords: palladium, core-shell nanoparticles, hexadecylamine, fuel cells,.

## 1. Introduction

The electro-oxidation of alcohols and most particularly of methanol has been investigated extensively given its great potential in energy-saving technologies such as that of direct methanol fuel cells (DMFCs). DMFC is a potential candidate for power generation due to high energy conversion efficiency, low operation temperature, low pollutant emission, ease of storage and low cost [1]. The application of DMFC is restricted by two main disadvantages in conventional anodic catalysts supported on carbon (such as Pt/C), namely high cost and sluggish kinetics of methanol electro-oxidation at low temperatures. Consequently, current research is oriented towards the development of alternative catalysts containing low amounts of Pt or even non-Pt catalysts [2]. In this regard, Pd-based catalysts are of interest due to their high activity for the electro-oxidation of alcohols in alkaline media [3-7]. Furthermore, Pd is more abundant than Pt, thus justifying the current intensive researches with this metal.

The synthesis of palladium nanoparticles onto various carbon and non-carbon supports has been widely studied. Different chemical methods are used including the use of organic molecules to stabilize the particles and limit their agglomeration. Depending on the stabilizer used for the synthesis of the metal nanoparticles, the interaction stabilizer-surface can be through a strong covalent linkage, chemisorbed atom or electrostatic [8]. Some investigations demonstrated that the stabilizers can modify the surface state of metal nanoparticles and consequently, their surface properties, offering thus a way to tune them [9,10]. This is interesting considering catalysis as application since a stabilizing ligand can be chosen to influence the catalytic properties of the particles. However, a right balance is needed between the ability of a ligand to stabilize metal nanoparticles and the accessibility of reactant molecules to their surface for the catalysis to happen [11]. Table 1 provides some of the main methods reported for the fabrication of protected-Pd nanoparticles using various organic molecules as stabilizers [3-5,11-34], such as PVP, ethylene glycol, phosphines, amines, alcohols, thiols, etc. However, less common stabilizers such as symmetric diphosphites or alkylether N-substituted pyrazole ligands and others have been employed focusing to specific catalytic applications. Some reported facts indicated that appropriate surface modification of metal nanoparticles might improve their electrocatalytic activity for a given electrochemical reaction [25]. The nature of metal precursors is important to obtain metal nanoparticles with well-defined characteristics. Pd-nanoparticles have been generally synthesized by the chemical reduction of Pd salts and organometallic precursors have been rarely used, Table 1. However, the synthesis of Pd nanoparticles using Pd(acac)<sub>2</sub> provided more monodisperse distributions of Pd-nanoparticles than chloride salts. In addition, the carbon monoxide generated in situ from the decomposition of the acac ligands is crucial to control the particle growth process [23]. An alternative to Pd(acac)<sub>2</sub> is the Pd<sub>2</sub>(dba)<sub>3</sub> organometallic complex. The decomposition of

this precursor under hydrogen in the presence of weakly coordinating ligands like amines as stabilizers is known to generate Pd-nanoparticles that are controlled in size and dispersion [31].

In the present work, we report on the use of the organometallic approach for a one-pot synthesis of a Pd-nanocatalyst dispersed onto Vulcan carbon, starting from Pd(dba)<sub>2</sub> as the metal source and using by hexadecylamine as a stabilizer. This synthesis method allowed to obtain a Vulcan-supported Pd-nanomaterial made of ca. 4.5 nm in size Pd nanoparticles that are well-dispersed on the carbon matrix. When this nanomaterial was heat-treated at 400°C under air, a core-shell Pd@PdO structure was obtained. A comparison study of the two nanomaterials, Pd/HDA/C and Pd/HDA/C@air-ht, has been performed for the methanol electro-oxidation reaction.

## 2. Experimental

### *2.1 Synthesis of vulcan-supported HDA-stabilized Pd-nanoparticles*

All experiments were carried out using standard Schlenk tube or Fischer-Porter bottle techniques under nitrogen (99.998%, INFRA). Bis(dibenzylideneacetone)palladium(0), Pd(dba)<sub>2</sub> (99%, Sigma-Aldrich), hexadecylamine, CH<sub>3</sub>(CH<sub>2</sub>)<sub>15</sub>NH<sub>2</sub> (98%, Sigma-Aldrich) and dihydrogen, H<sub>2</sub> (99.997%, INFRA) were used as metal source, stabilizer and reactive agent, respectively. Anhydrous THF and pentane (99.9%, Sigma-Aldrich) were used as solvents under nitrogen.

In a typical synthesis, 0.783 mmol of Pd(dba)<sub>2</sub> and 1.56 mmol of HDA (1:2 molar ratio Pd:HDA) were dissolved in 60 mL of THF under nitrogen atmosphere in a Fisher-Porter bottle containing Vulcan carbon (XC-72R; 90 wt.%). The reaction mixture was then pressurized with dihydrogen (3 bar) and left to react (20 h) at room temperature (r.t.) under vigorous stirring, Figure 1. The dihydrogen excess was then eliminated and the reaction mixture concentrated by solvent evaporation under vacuum. The addition of anhydrous pentane to the suspension allowed to separate the Pd-nanomaterial which was purified by a washing/filtration sequence (3 times with 20 mL of pentane). Finally, a drying under vacuum led to a black powdery solid named Pd/HDA/C (10 wt.% Pd, nominal). In a second step, the obtained Pd/HDA/C nanomaterial was heat-treated at 400 °C in air for 2 h which led to Pd/HDA/C@air-ht nanomaterial [31]. The heat-treatment was carried out in order to provide core-shell nanoparticles. The two Pd-nanomaterials were characterized and evaluated in methanol electro-oxidation reaction in alkaline medium for comparison purpose at fuel cell systems.

### *2.2 Characterization techniques of the materials*

Phase identification, crystallite sizes and changes in lattice parameters were determined by powder-X-ray diffraction (XRD) and Rietveld refinements. XRD data acquisition was performed from 10 to 90° 2-theta range in a D2 Phaser Bruker diffractometer using CuK $\alpha$  radiation in Bragg-Brentano theta-theta configuration. All Pd samples including Pd/C ETEK (30 wt.%) were measured using an alumina internal standard to improve accuracy in the measures of 2-theta displacements. Reflections in alumina standard (PDF 01-070-5679) do not interfere in the Pd or PdO identification. Rietveld refinements were carried out using TOPAS V5 software where the double-Voigt model was selected to estimate crystallite size.

Samples for transmission electron microscopy (TEM) characterization were prepared by dropping an isopropanol dispersion of purified black solid Pd/HDA/C or and Pd/HDA/C@air-ht, onto holey carbon-covered copper grids. High resolution transmission electron microscopy (HR-TEM), scanning transmission electron microscopy (STEM) and electron energy loss spectroscopy (EELS) results were collected on a JEM-ARM 200CF microscope operating at 200 kV. The STEM probe of ca.1.0 nm at FWHM, 1.2 nA probe current and the EEL spectra were collected with 0.25 eV dispersion per channel. The HR-TEM images were analyzed with Digital Micrograph software. The average particle was estimated from 150 nanoparticles captured in 18 images. The EEL spectra were obtained and analyzed with Cornell Spectrum Imager (CSI) [36]. The backgrounds in the EEL spectra were subtracted using standard methods [37] and smoothed in an interval from 200 to 712.25 eV.

In order to determine elemental composition of the palladium nanocatalysts, X-ray photoelectron spectroscopy (XPS) was carried out using a K-alpha from Thermo Fischer Scientific spectrometer with a monochromatic Al K $\alpha$  X-ray source (1486.6 eV). The X-rays were microfocused at the source to give a spot size on the sample of 400  $\mu$ m of diameter. Samples remained under vacuum for more than 10 h in a pre-chamber directly connected to the equipment. After that, they were transferred to the analysis chamber where a pressure of  $1 \times 10^{-9}$  Torr remained constant during all the experiments. The pass energy for the survey and high-resolution spectra was set to 160 and 45 eV, respectively. The C1s peak at 284.5 eV was used as internal standard in order to compensate effects related with charge shift. Core-level spectra were deconvoluted for each component using a pseudo-Voigt function with Gaussian (70%) - Lorentzian (30%) functions and a Shirley-type background with AVANTAGE V5.97 software from Thermo Fisher Scientific.

### *2.3 Electrode preparation and electrochemical measurements*

Electrochemical measurements were performed using a potentiostat-galvanostat (Versastat 3) in a conventional three-electrode cell. A glassy carbon rod (GCE; 3.0 mm in diameter) previously polished with alumina powder (ca. 0.3  $\mu\text{m}$ ) and washed ultrasonically in 18.2 M $\Omega$  deionized water (D.I. water), was used as a substrate for the working electrode. A reversible hydrogen electrode (RHE) prepared with 0.5 M H<sub>2</sub>SO<sub>4</sub> and a platinum wire were used as reference and counter electrodes, respectively. The Pd/HDA/C, Pd/HDA/C@air-ht (9:1 wt.% ratio Vulcan carbon: total metal 10 wt.%-metal) and Pd/C ETEK (7:3 wt.% ratio Vulcan carbon: total metal 30 wt.%-metal) catalytic suspensions were prepared by mixing Nafion, isopropanol and D.I. water (1.070 mL) under ultrasounds. The current magnitude was normalized with respect to mass activity for comparison purpose between prepared Pd-nanomaterials and commercial Pd/C ETEK sample. Thereafter, 5  $\mu\text{L}$  of each prepared suspension was deposited onto the mirror-finish glassy carbon substrate and dried at room temperature under an argon atmosphere. The metallic loading in the working electrode for Pd/HDA/C and Pd/HDA/C@air-ht was ca. 33.05  $\mu\text{g cm}^{-2}$ . The current *versus* potential characteristics (*i*-*E*) of the catalysts were recorded in 0.5 M KOH solution, previously degassed with Ar bubbling, at a scan rate of 100 mV s<sup>-1</sup> using cyclic voltammetry (CV) in a potential window from -0.72 to 0.43 V/RHE, starting at open circuit potential. The *i*-*E* characteristics as a function of alcohol concentration (0.001, 0.01, 0.1 and 1.0 M) in the alkaline environment were obtained at 5 mV s<sup>-1</sup>. The solutions were purged with argon for 15 min prior to electrochemical analysis.

The electrochemical active surface area (ECSA) from the absorbed monolayer of PdO<sub>red</sub> for each catalyst was calculated using CV measurement in a solution of 0.5 M KOH from -0.72 to 0.88 V/RHE at a scan rate of 50 mV s<sup>-1</sup>.

Whereas, an activation of the electrode in turn (in 0.5 M KOH at a scan rate of 50 mV s<sup>-1</sup> at room temperature) was performed for the CO-adsorption-desorption reaction (CO-stripping) in a potential window from -0.72 to 0.43 V/RHE.

For such an approach, the electrochemical cell was saturated with CO gas for 5 min with a bias-potential of -0.57 V/RHE. After that, argon was bubbled into the electrolyte for 20 min to remove the CO dissolved and a CV was conducted at a scan rate of 5 mV s<sup>-1</sup>.

On the other hand, the electrochemical impedance spectroscopy (EIS) characterization of the two Pd-nanomaterials was carried out in 0.5 M KOH solutions containing 1 M CH<sub>3</sub>OH. This study was performed by applying a sinusoidal signal of 10 mV amplitude and a frequency range from 100 kHz to 10 mHz, using a Versastat 3 equipment. These measurements were recorded at OCP (open circuit

potential) and by imposing -0.02, 0.08 and 0.18 V/RHE more positive than the OCP. The behavior of the commercial catalyst Pd/C (from ETEK) in similar conditions is shown for comparison purpose.

### 3. Results and Discussion

#### 3.1 X-Ray diffraction analysis

XRD results of Pd/HDA/C, Pd/HDA/C@air-ht nanomaterials and a commercial sample (Pd/C ETEK) are presented in Figure 2. For the afore-mentioned XRD patterns, alumina Al<sub>2</sub>O<sub>3</sub> (JCPDS 01-070-5679) was used as internal standard. Additionally, data for Vulcan carbon before and after heat treatment are also shown as references in order to prove its thermal stability. XRD patterns of Pd/HDA/C, Pd/HDA/C@air-ht and Pd/C ETEK confirmed the presence of face-centered cubic (FCC) crystal structure of palladium successfully supported onto Vulcan carbon. Four main broad diffraction peaks were observed at  $2\theta = 40.07^\circ$ ,  $46.73^\circ$ ,  $68.12^\circ$  and  $82.12^\circ$  corresponding to (111), (200), (220) and (311) planes (JCPDS 00-046-1043), respectively. For the Pd/HDA/C@air-ht nanomaterial, additional diffraction peaks corresponding to palladium oxide (JCPDS 00-041-1107) are visible at  $2\theta = 33.97^\circ$ ,  $41.97^\circ$ ,  $54.81^\circ$ ,  $60.39^\circ$  and  $71.67^\circ$  assigned to (101), (110), (112), (103) and (202) planes, respectively. The presence of PdO could be expected due to the heat-treatment in air undergone for this sample. Quantitative phases analysis carried out by Rietveld revealed that PdO is presented at 61.80 % in the Pd/HDA/C@air-ht sample. Conversely, Vulcan support pattern shows two broad peaks of low intensity between 10 and 30° ( $2\theta$ ) [38]. Furthermore, crystallite sizes calculated by the double-Voight model included in the Rietveld refinement are given in Table 2. According to these results, crystallite size of catalysts heat-treated at 400 °C in air (41.72 nm) increased in comparison with Pd/HDA/C (4.5 nm). This increment in crystallite size could be due to (i) the elimination of HDA by thermal decomposition that may let a relative agglomeration of Pd-nanoparticles and (ii) the formation of a Pd@PdO core-shell structure, attributed to the oxidation of Pd under air [35,39], as can be seen in HR-TEM/STEM-EELS analyses.

#### 3.2 Electron microscopy analysis

TEM micrographs and the corresponding size distributions of Pd/HDA/C and Pd/HDA/C@air-ht nanomaterials are presented in Figures 3a-b. From TEM images, Pd-nanoparticles appear darker as compared to Vulcan carbon due to difference in their atomic number; in addition, the observed particles are semi-spherical and well-dispersed on the carbon support. Furthermore, these

nanoparticles exhibit a narrow particle size distribution centered at ca.  $4.5 \pm 1.02$  nm. On the other hand, the calculated crystallite size obtained from XRD analysis is in the same order of magnitude (i.e. 4.5 nm). Conversely, for Pd/HDA/C@air-ht nanomaterial presents a particle size distribution centered at ca.  $10 \pm 1.79$  nm as determined by TEM. Whereas, the calculated crystallite size obtained from XRD analysis was 41.72 nm, Table 2. According with some fundamentals on the XRD technique, the diffraction occurs from a considerable volume of the sample and powders are normally not monodisperse. Thus, the polydispersity of nano-powders is not considered in Rietveld method [40,41]. In the opposite, TEM technique will allow the analysis of well dispersed and better crystallized nanoparticles. To complete the characterization of the samples, a series of experiments were carried out using HR-TEM, STEM and EELS. In the HR-TEM images of the Pd/HDA/C and Pd/HDA/C@air-ht catalysts, Figures 3c-d, lattice fringes are observed, indicating that the samples present crystalline nature. Fast Fourier Transform (inset Figure 3c) from the marked particle is indexed as  $(\bar{2}00)$ ,  $(2\bar{2}0)$  and  $(0\bar{2}0)$  planes with the orientation along  $[001]$  axis zone, which evidences the presence of FCC phase of metallic palladium nanoparticles. In the opposite, Figure 3d shows two different interplanar distances at 2.24 and 2.15 Å corresponding to Pd and PdO phases which are related to the crystal planes (111) and (110), respectively. From these data, it thus appears that the sample heat-treated at 400 °C presents an oxygen-rich shell over the metallic-palladium core, which can explain the increment of the particle size observed compared to that in Pd/HDA/C. The existence of core-shell structures in Pd/HDA/C@air-ht catalyst was confirmed by STEM-EELS analyses. STEM images and the corresponding compositional EELS maps of Pd/HDA/C and Pd/HDA/C@air-ht catalysts are shown in Figures 4a-b. EELS spectra acquired from regions marked in Figures 4a-b are presented in Figures 4c-d. Spectrum (1) of both catalysts is acquired from the support Vulcan carbon, showing K edge peak at 285 eV due to the excitation of  $\pi^*$  states [42,43] and edge peak at 290 eV of  $\sigma^*$  states [44], linked with the intrinsic nature of Vulcan, usually composed of  $sp^2$  or  $sp^3$  hybrid forms [45]. The spectra 2 (Figure 4d) acquired from the edge particle of Pd/HDA/C@air-ht catalyst indicates the presence of PdO with a peak around 532 eV (oxygen K-edge). In spectrum (3) acquired from the center of the particle (Figure 4d), only one peak at 335 eV ( $Pd:M_{4,5}$ ) is observed that can be assigned to metallic Pd. Figure 4c displays the EEL spectra from edge (2) and center (3) acquired for Pd/HDA/C. From this, features related with metallic Pd (335 eV) are observed. The composite map of Pd/HDA/C (inset Figure 4a) presents a quasi-homogeneous intensity across the mapped area that corresponds to metallic Pd (green), except for a few spots in red that could be assigned to oxygen adsorbed from the atmosphere. In contrast, the inset in Figure 4b shows the composite map of Pd/HDA/C@air-ht catalyst exhibiting chemical heterogeneity. The center of the particle appears with higher palladium intensities (green) while the

edge shows oxygen (red), confirming a core-shell structure (Pd@PdO). Both composite maps show carbon marked in blue. So, the heat treatment at 400°C in air undergone by the Pd/HDA/C nanomaterial did not result in the complete oxidation of Pd(0) to PdO species into the Pd/HDA/C@air-ht catalyst; as it has been reported in other works [35]. It is therefore possible that the diffusion of oxygen atoms into the Pd lattice was carried out only onto the surface layers, as a result of the dissociative oxygen-adsorption on the particle surface. It has been reported in some investigations that temperatures near 400 °C do not upshot the oxidation of the core making a stable PdO layer [35], supporting the presence of Pd@PdO core-shell-like structures when heat treated under air. Hence, as it will be seen later on, the formation of such a core-shell structures improved the catalytic activity due to an important increment in the surface area, leading to a better reaction performance in comparison with the Pd/HDA/C catalyst, as demonstrated by electrochemical evaluation.

### 3.3 X-Ray photoelectron spectroscopy (XPS)

The interactions between surface chemical states of the prepared nanomaterials were determined by XPS. In supplementary information, Figure S1 shows the comparison of the relative intensities of C1s, O1s, N1s and Pd3d in the XPS survey spectra for Pd/HDA/C and Pd/HDA/C@air-ht and the elemental quantification of the carbon-supported Pd-nanomaterials are given in Table 3. In XPS spectrum of Pd/HDA/C@air-ht sample, the O1s signal is stronger than in the case of Pd/HDA/C. The elementary quantification of the core-shell particles (Pd/HDA/C@air-ht), Table 3, shows that there is a higher oxygen content in the shell than in the cores of the particles. This can be explained by shell constituted mainly by palladium oxide or Pd-O species while in the cores, metallic palladium is the dominant species [46]. These results are in agreement with the results from HR-TEM/STEM-EELS. To determine in more detail the oxidation states and chemical species in Pd/HDA/C and Pd/HDA/C@air-ht nanomaterials, high-resolution XPS spectra for the Pd3d were acquired and subsequently analyzed by deconvolution modeling. According to this, the asymmetric characteristics of the Pd3d main orbital signals, Pd3d<sub>5/2</sub> and Pd3d<sub>3/2</sub>, in the interval from 333.5 to 346.7 eV suggest the presence of species with different Pd-oxidation states. XPS narrow spectra (Figure 5) were fitted with five double spin-orbit components with the set of Pd species (Pd(0), PdO, PdO<sub>2</sub>, Pd-C) and parental species as reported in Table 4. The first contribution of the Pd3d region at 335.2 and 340.4 ± 0.2 eV for Pd3d<sub>5/2</sub> and Pd3d<sub>3/2</sub> peaks, is assigned to Pd(0) [47-67]. The second spin-orbit component corresponds to PdO where Pd3d<sub>5/2</sub> is located at 336.9 ± 0.2 eV and Pd3d<sub>3/2</sub> at 342.1 ± 0.2 eV [47,49-51,53,55-59,61-65,67,68]. As can be seen, the difference in the

core-level binding energy between the Pd (0) and Pd (II) spin-orbit components is 1.7, in agreement with the literature data [61]. Nevertheless, the PdO contribution presents two satellites, SI and SII, located at 339.4 eV and  $345.5 \pm 0.2$  eV, respectively. The nature of SI peak is still unclear [55], while the SII peak is generated from charge transfer processes that are induced by the palladium [59]. In this way, the binding energy of components are in good agreement with other studies, which verify that SI and SII are at an energy distance of about 2.6-2.65 eV and 8.6-9.0 eV with regard the PdO main line [55,59,61].

Moreover, the third contribution is related with PdO<sub>2</sub> at 337.7 and  $342.9 \pm 0.2$  eV, associated to Pd3d<sub>5/2</sub> and Pd3d<sub>3/2</sub>, respectively; these are assigned to the formation of surface species of Pd (IV) [49,55,56,58,61,69,70-72]. It suggests that the formation of PdO<sub>2</sub> species in the surface of the nanostructures is associated with the Pd oxidation when the samples are in contact with air [39]. As previously reported, an oxide layer may formed when a metal surface is exposed to an oxygen-containing atmosphere even at low temperature and pressure [73]. Considering the quantification of both samples, these species (PdO<sub>2</sub>) are less than 2%, below the detection limit of XRD and HR-TEM/STEM-EELS techniques; linked with its poor distribution in the support-carbon matrix. However, the fourth spin-orbit component is associated to the interaction Pd-C at 336.0 and  $341.2 \pm 0.2$  eV [52,66] for Pd3d<sub>5/2</sub> and Pd3d<sub>3/2</sub>. Whereas, the fifth contribution could be related to the parental species, which are traces from the precursor located between 338.45 and  $338.60 \pm 0.2$  eV.

It is noteworthy in Figure 5 that the Pd3d spin-orbit components of Pd/HDA/C@air-ht nanomaterial show a shift towards higher binding energies. This is induced by a change in electronic properties, which can be attributed to i) the presence of palladium-oxides species in a highest proportion with respect to the Pd/HDA/C sample, and ii) some interactions between Pd and PdO in the Pd@PdO [74] core-shell particles, as demonstrated by HR-TEM/STEM-EELS. Then, this analysis also suggests that the metallic-palladium surface at the material labeled Pd/HDA/C@air-ht is covered with a PdO layer formed during heat-treatment linked with (i) the migration of atoms, which is more efficient at higher temperatures [35,50] and (ii) the difference of the surface tensions that avoids the dissolution between the metallic Pd and the PdO, as has been reported elsewhere [50]. In addition, the deconvolution results of the Pd3d high-resolution XPS spectra indicate that the content of palladium oxides in Pd/HDA/C is significantly lower than in Pd/HDA/C@air-ht, Table 4. Therefore, the XPS results suggest that the highest catalytic activity (vide infra) can be due to the fact that a greater number of electrochemical active sites are promoted by the PdO species present on the surface in the sample heat-treated at 400 °C in air as demonstrated in the electrochemical evaluation, see next section.

### 3.4 Electrochemical evaluation

In this section, the electrochemical characterization of Pd/HDA/C, Pd/HDA/C@air-ht and Pd/C ETEK catalysts is presented. The as-synthesized materials were evaluated in the oxidation reaction of methanol in alkaline media for fuel cell applications and compared to commercial P/C ETEK.

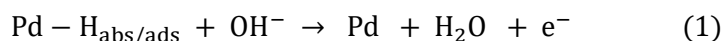
#### 3.4.1 Cyclic voltammetry

Electrochemical studies of the Pd nanomaterials supported onto Vulcan have been performed using a solution containing 0.5 M KOH previously deaerated with argon gas. In Figure 6 the *i-E* characteristics obtained from the current response in a potential window from -0.72 to 0.43 V/RHE at r.t. at and scan rate of 100 mV s<sup>-1</sup> are plotted, initiating from the open circuit potential toward positive-going scan. The Pd electro-catalysts show regions of hydrogen adsorption/desorption at the potential interval from -0.72 to -0.27 V/RHE (zone I, II), Figure 6. An OH<sup>-</sup> species-adsorption peak that appears in the positive-going scan at the potential interval from -0.24 to -0.12 V/RHE (zone III) in Pd/HDA/C@air-ht and Pd/C ETEK catalysts, can be attributed to the formation of palladium (II) oxide (PdO) or hydroxide-metal (Pd-OH<sub>ads</sub>) on the surface [75,76]. The OH<sup>-</sup> ions are first chemisorbed during the initial stage of the oxide formation, supplying electrons at more positive potentials, resulting in the formation of higher-oxidation-state species [77].

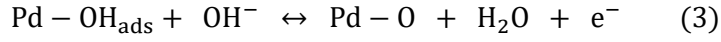
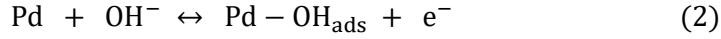
These adsorbed OH-species could, in fact, promote a better organic (i.e. methanol) oxidation-performance, decreasing the CO-like poisoning, producing carbon dioxide and other carbonaceous species [38].

On the other hand, the peak at ca. -0.04 V/RHE (zone IV) is attributed to the formation of palladium (II) oxide [77]. Whereas the well-defined peak in the negative-going scan from ca. -0.34 to 0.16 V/RHE (zone V) denotes reduction process from palladium oxide/hydroxide species formed during the positive-going scan [75,77]. The reaction sequence for the oxidation-reduction processes on Pd-catalysts in alkaline media is observed in equations (1-5) [77].

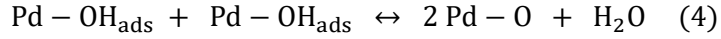
Zones I - II



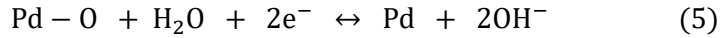
Zone III



Zone IV



Zone V



It is important to note that the current magnitude of the reduction peak at Pd/HDA/C@air-ht is higher than that in its counterpart Pd/HDA/C and Pd/C ETEK materials; this suggests that (during polarization) more metal-oxides/hydroxides surface-species are available in order to increase the ECSA [46]. In this context, the determination of the ECSA was calculated in order to evaluate the catalytic activity in CH<sub>3</sub>OH oxidation [78]. Hence, the ECSA was calculated with the charge obtained during the induced PdO<sub>red</sub> and in the CO-stripping reactions. In the case of the PdO<sub>red</sub> ECSA-approach, Figure S2 displays the *i*-*E* characteristics for the catalysts in study at different switching potentials (*E*<sub>λ</sub>, from 0.33 to 0.88 V/RHE) with the corresponding profiles *Q* versus *E*<sub>λ</sub>, see insets; from the intersection of these slopes (*Q*<sub>PdO</sub>, related with the formation of a PdO monolayer[79]) the charge can be obtained.

The ECSA was determined taking into account that the amount of charge for the reduction of a Pd (II)-oxide monolayer is 420 μC cm<sup>-2</sup> [80], equation (6) [46,81,82].

$$ECSA_{\text{PdO}}(\text{m}^2\text{g}^{-1}) = \left[ \frac{Q_{\text{PdO}}(\text{C})}{S(\mu\text{C cm}^{-2}) \cdot l(\text{mg})} \right] 10^5 \quad (6)$$

Where *Q* is the charge (C), *S* is the conversion factor used to relate charge with the surface area (μC cm<sup>-2</sup>) and *l* is the amount of Pd-catalyst loaded (mg). The calculated active surface area was in the order 143.69 (Pd/HDA/C@air-ht) > 118.89 (Pd/C ETEK) > 91.10 (Pd/HDA/C) in m<sup>2</sup> g<sup>-1</sup>.

In addition, using equation (7) [83], the ECSA was calculated from the CO-stripping reaction at the electrode interface, in the alkaline environment (0.5 M KOH) Figure S3. Peaks attributed to CO-oxidation to CO<sub>2</sub> and located at ca. -0.08, -0.01 and 0.07 V/RHE for Pd/HDA/C@air-ht, Pd/C ETEK and Pd/HDA/C, were observed.

$$ECSA_{CO}(\text{m}^2\text{g}^{-1}) = \left[ \frac{Q_{CO} (\text{C})}{420 \mu\text{C cm}^{-2} L_{Pd} (\text{mg cm}^{-2}) A_g (\text{cm}^2)} \right] 10^5 \quad (7)$$

In the equation,  $Q_{CO}$  is the charge for the CO-induced adsorption (after subtraction of the double layer) and with  $0.420 \text{ mC cm}^{-2}$  corresponding to a monolayer of adsorbed CO [84];  $L_{Pd}$  is the Pd-catalyst loading on the working electrode and  $A_g$  is the geometric surface area of the glassy carbon electrode. As in the case of a PdO monolayer adsorption-desorption ( $ECSA_{PdO}$ ), the ECSA during CO-stripping ( $ECSA_{CO}$ ) was in the same order, as expected. The calculated ECSA and the obtained  $CO_{ad}$  stripping-reaction parameters (i.e. onset potential ( $E_{onset-CO}$ ), peak potential ( $E_{CO}$ ) and peak current ( $I_{CO}$ )) are reported in Table 5. In summary, the heat-treated material induces a better adsorption-desorption phenomenon for CO-stripping (low CO-poisoning effect), See Figure S3, associated with i) the reaction-overpotential, ii) peak-current potential onset, iii) a higher current-oxidation magnitude and iv) a major OH-adsorption due to the presence of PdO species surrounding the metallic palladium in the core-shell.

Moreover, as it can be seen, the magnitude of the electrochemical active surface area calculated by  $PdO_{red}$  with respect to that calculated using CO-stripping reaction are similar. According to these results, the Pd/HDA/C@air-ht catalyst displays an ECSA value 1.6 and 1.2 times higher than Pd/HDA/C and Pd/C ETEK, respectively. Although, it has been mentioned that the presence of palladium oxide species inhibits the CO-oxidation reaction [85], in our study, it appears that the heat-treated catalyst presents a better performance as a consequence of the formation of core-shell array and interaction between the Pd and PdO species that promote a major number of electrochemical active sites on the surface of the nanoparticles as revealed using HR-TEM/STEM-EELS and XPS techniques.

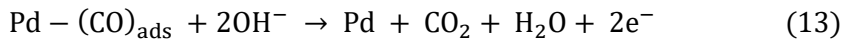
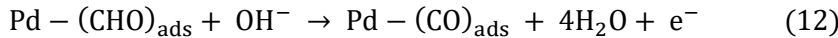
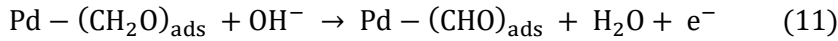
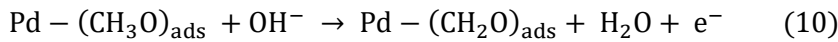
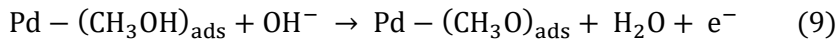
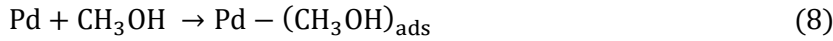
On the other hand, an additional oxidation process of PdO is observed at more anodic overpotentials, Figure S2; resulting in the formation of some others species with a higher oxidation state (such as  $PdO_2$ ). This result is supported by XPS data. In this context, at Pd/HDA/C@air-ht catalyst the peak observed at ca. 0.58 V/RHE, could be attributed to the reduction of  $PdO_2$  species [86, 87], see inset in Figure S2. In addition, the current magnitude of those redox-peaks is slightly higher for Pd/HDA/C@air-ht catalyst in comparison to that observed with its counterparts. According with literature data, these higher oxidation state species did not induce a negative effect on the catalytic activity [88].

### 3.4.2 Methanol oxidation reaction (MOR)

The electrochemical performance of the prepared materials during MOR was carried out using cyclic voltammetry in 1 M CH<sub>3</sub>OH, and 0.5 M KOH as electrolyte. Typical *i-E* characteristics are observed plotted in Figure 7. From these profiles, it is possible to observe that the sample heat-treated displays the highest faradic current (Figure 7a), followed by the commercial catalyst and the untreated-prepared sample.

In addition, the peak potential variation ( $E_p$ ) during the positive-going scan (attributed to the oxidation of chemisorbed CH<sub>3</sub>OH species, forming intermediates as a result of methanol-dehydrogenation, including CO and CO<sub>2</sub>) was 0.22, 0.11 and 0.12 V/RHE for Pd/HDA/C@air-ht, Pd/HDA/C and Pd/C ETEK, respectively.

On the other hand, during the negative-going scan the observed current could be attributed to an incomplete removal of adsorbed-surface intermediates (carbonaceous species) generated during the positive-going scan [81,82]. A possible pathway for CH<sub>3</sub>OH oxidation reaction in an alkaline medium is represented by equations (8-13) [81]:



As can be seen, the CH<sub>3</sub>OH electro-oxidation mechanism is a six-electron process. It is noteworthy that the chemisorption of methoxy species weaken the CO-bond on the surface of Pd-catalyst with the adsorbed methanol [75]; carbonate ions can be also formed due to the alkaline environment [89]. The magnitude of the current for the Pd/HDA/C@air-ht catalyst is 5.4 times higher than that of commercial Pd/C ETEK catalyst. This difference in activity might be related to the presence of PdO, resulting in an improvement in the catalytic activity and in the decrease of the overpotential. Moreover, the relationship between the current magnitude during the positive-going scan ( $I_f$ ) and the negative-going scan ( $I_b$ ) can be used to establish the tolerance to some CO-accumulation and other carbonaceous species (poisoning due to intermediate-adsorbed species).

As shown in Table 6, the calculated  $I_f/I_b$  for the catalysts, at scan rate of 5 mV s<sup>-1</sup> were 1.53, 1.45 and 1.69 for Pd/HDA/C@air-ht, Pd/HDA/C and Pd/C ETEK, respectively. The Pd/HDA/C@air-ht catalyst showed a higher value than its counterpart Pd/HDA/C. Therefore, the surface of this

catalyst is effective in the removal and/or anti-poisoning capability of carbonaceous species (including CO) during the positive-going scan [82,90], as confirmed by CO-stripping reaction in this study. According to this, it can be established that the core-shell structure-array plays an important role in the redox process, presenting good stability and high resistance to poisoning by adsorbed species; being an interesting alternative for applications in fuel cell systems [60]. Linked with this, the onset potential ( $E_{\text{onset}}$ ) is another parameter to evaluate the catalytic activity of a catalyst [51]. In this context, the  $E_{\text{onset}}$  of the catalysts is in the order Pd/HDA/C > Pd/C ETEK > Pd/HDA/C@air-ht, Table 6; suggesting that the overpotential decreases in the core-shell system, accelerating the oxidation/removal of the generated species during MOR. Moreover, the onset potential decreases as the concentration of CH<sub>3</sub>OH increases in all catalysts, evidencing that the electro-oxidation reaction presents less overpotential at high concentrations of CH<sub>3</sub>OH, see insets in Figure 7a.

From the  $i$ - $E$  profiles obtained at different CH<sub>3</sub>OH concentrations (0.001, 0.01, 0.1 and 1 M) at a scan rate of 5 mV s<sup>-1</sup>, Figures 7b-d, two parameters during the positive-going scan were obtained: peak potential ( $E_p$ ) and peak current ( $i_p$ ). For example, in Figure 7b, the variation of the  $E_p$  versus methanol concentration is presented. It is interesting to observe that the potential becomes more positive as a function of concentration, due to mass transport limitations [81] regardless the material in turn. This variation is in the order Pd/HDA/C@air-ht > Pd/C ETEK > Pd/HDA/C, as expected. Furthermore, the Pd/HDA/C and Pd/C ETEK catalysts show higher overpotentials with respect to the onset potential in Pd/HDA/C@air-ht. On the other hand, the dependence of the peak current ( $i_p$ ) with concentration of methanol is plotted in Figure 7c. For all samples in study, the faradic current increases with concentration and its magnitude is in the order Pd/HDA/C@air-ht > Pd/C ETEK > Pd/HDA/C; indicating a better charge-transfer process in the core-shell system.

As a resume, the charge variation ( $Q$ ) as a function of the concentration of CH<sub>3</sub>OH is shown in Figure 7d. The charge at Pd/HDA/C@air-ht is higher than in Pd/C ETEK and Pd/HDA/C catalysts. This charge increases with respect to methanol concentration for Pd-catalysts, suggesting an improvement in the catalytic activity; representing those species that are generated in the electro-oxidation, including intermediaries and products. This result is attributed to the presence of PdO species, which modified the electronic properties (as demonstrated by XPS analysis) promoting more efficient redox processes at the interface for the deprotonation of CH<sub>3</sub>OH.

### 3.4.3 EIS characterization of Pd-based catalysts for methanol oxidation reaction

In Figure 8 are shown the impedance diagrams recorded at open circuit potential (OCP) and by imposing -0.02, 0.08 and 0.18 V/RHE during methanol oxidation. The apparent formation of semicircles for the different catalysts can be noted in the Nyquist diagrams (Figures 8a,c,e), reaching similar values in the order of  $k\Omega$ , and decreasing in diameter as the potential becomes more positive. It is important to notice that the impedance values are larger for Pd/HDA/C even during polarization toward more positive values, Figure 8a. Conversely, in the case of Pd/HDA/C@air-ht and Pd/C ETEK the impedance values decrease one and two orders of magnitude during the applied potential at 0.08 and 0.18 V/RHE (see inset, Figures 8c,e) indicating a rapid oxidation of methanol.

Similar responses are evident in the Bode diagrams (phase angle vs frequency, Figures 8b,d,f) where a resistive behavior at high frequencies was observed, reaching a maximum at intermediate frequencies. This capacitive contribution is maximum at OCP. When more positive potentials were applied, these phase angles decrease with potential. At high frequencies, the resistive contribution of the Pd/HDA/C@air-ht and Pd/C ETEK catalysts is observed in three frequency-decades with respect to Pd/HDA/C. On the other hand, a decrease in the phase angles is observed at low frequencies, being evident an inductive-like behavior (see insets in, Figures 8d,f).

According to these results the MOR using Pd-based catalysts is different as a consequence of i) the electrode-polarization (catalysts and substrate) and ii) a mass-transport process of the electroactive species (methanol). The lower impedance values put in clear that Pd/HDA/C@air-ht and Pd/C ETEK are the best catalyst for the reaction in turn. Whereas for the Pd/HDA/C catalyst a low oxidation-current of the probe molecule is given due to high impedance values (resistive-like behavior). It is presumed that the MOR on these catalysts depends on different aspects such as particle size, chemical composition, structure and morphology (i.e. core-shell array) and the interaction of the catalysts with the carbon substrate.

To further discuss the electrochemical behavior of the Pd nanocatalysts in the MOR, the EIS diagrams recorded for Pd/HDA/C, and some cases for Pd/HDA/C@air-ht and Pd/C ETEK, were simulated using the circuit sketched in Figure 9a; whereas, those diagrams displaying the inductive behavior (Pd/HDA/C@air-ht and Pd/C ETEK) were fitted using the equivalent circuit in Figure 9b. These equivalent circuits considered the following contributions i)  $Q_1-R_1$  and  $Q_2-R_2$  that are linked with the methanol oxidation reaction on the catalysts and/or the substrate; and ii) the arrangement  $Q_{ads}-R_{ads}$  or  $L_{ads}-R_{ads}$  that is related with an adsorption process on the catalysts. This adsorption could be assigned with methanol and/or other species such as CO or CO<sub>2</sub>. The parameters obtained are listed in Table S1. As can be seen, a slight variation in the solution resistance is recorded. These

results are in the same order of magnitude with respect to the charge transfer resistance ( $R_{1,CT}$ ) reaching values of ca. 23  $\Omega$ , indicating a rapid methanol oxidation onto Pd-nanoparticles.

On the other hand, the electrical resistances ( $R_{2,CT}$ ) are different for Pd/HDA/C in comparison with those of Pd/HDA/C@air-ht and Pd/C catalysts. These differences could be due to the chemical composition of the catalysts as was observed from XPS analysis. In the case of Pd/HDA/C, metallic palladium was only detected being responsible of the methanol oxidation. Nevertheless, for both Pd/HDA/C@air-ht and Pd/C ETEK, the presence of other Pd-oxidation-states could be involved in the catalytic performance in agreement with the low resistance ( $R_{2,CT}$ ). Conversely, this oxidation is masked by the resistive contribution of the glassy-carbon substrate for the Pd/HDA/C. Additionally, during the polarization of the different Pd catalysts (Pd/HDA/C, Pd/HDA/C@air-ht and Pd/C ETEK) is likely to consider the adsorption of the methanol from the bulk towards the electrode ( $R_{ads}$ ). As was mentioned above, a low catalytic activity towards the methanol oxidation is expected for the Pd/HDA/C as the resistive contributions ( $R_{1,CT}$ ,  $R_{2,CT}$  and  $R_{3,ads}$ , see Table S1) are larger in comparison to those observed with Pd/HDA/C@air-ht and Pd/C ETEK. As shown in Figures 8d,f the marked difference is related with the inductive loop observed at low frequencies. This inductive response is commonly reported as a dissolution process (i.e. corrosion) or as an adsorption of different species on the substrate. In the case of the methanol oxidation, this contribution can be related with the adsorption of methanol and/or the adsorption of poisoning species. In the first case, the methanol could be easily oxidized having low impedance values and high oxidation-conversions; in the second case, the adsorption of CO or CO<sub>2</sub> (commonly related with a poisoning effect) could decrease the overall-process efficiency. Therefore, contribution from i) the existence of some palladium-oxidation states, ii) core-shell nano-particulated-array, and iii) particle size and distribution; avoid the poisoning for CO, enhancing the methanol oxidation on the synthesized Pd/HDA/C@air-ht and in the Pd/C from commercial source. Therefore, as the inductive response is enhanced at the interface of Pd/HDA/C@air-ht, related with a rapid transformation of methanol (see Table S1) its catalytic activity is better when compared with its counterparts employed in this study.

## Conclusions

In this work, a palladium-based nanomaterial, made of small Pd nanoparticles well-dispersed on Vulcan carbon (Pd/HDA/C) was successfully prepared starting from the organometallic Pd(dba)<sub>2</sub> precursor in one-pot conditions as well as its counterpart heat treated at 400 °C under air (Pd/HDA/C@air-ht). HRTEM-STEM-EELS characterization revealed i) the formation of well-dispersed Pd-based nanoparticles on the Vulcan-carbon support even after the heat treatment, and ii)

a Pd@PdO core-shell nanoparticle-array formation in the catalyst heat-treated in air at 400 °C. On the other hand, particle size determined from TEM analysis are centered at ca. 4.5 and 10 nm for Pd/HDA/C and Pd/HDA/C@air-ht, respectively. X-ray diffraction patterns showed a FCC-crystal structure for metallic palladium in all materials. However, the presence of Pd-oxide species in the case of Pd/HDA/C@air-ht was also observed. In addition, XRD data showed that the crystallite size for Pd/HDA/C@air-ht was 41.72 nm which is almost twenty times higher than that observed for Pd/HDA/C (ca. 2.04 nm). This difference can be attributed to the presence of PdO as a result of the heat treatment in air and the followed formation of a core-shell array, as demonstrated also from XPS analyses. STEM-EELS and XPS data evidenced the presence of PdO in the periphery of the particles thus forming core-shell P@PdO nanostructures. Electrochemical evaluation during cyclic voltammetry established well-defined transition-redox characteristics corresponding to palladium. It was found that methanol oxidation reaction (MOR) is possible at alkaline conditions in all set of catalysts evaluated. However, MOR-faradic current was more marked at the interface of Pd/HDA/C@air-ht due to the formation of a core-shell array that modifies the electronic-morphological and structural properties, improving the mass-charge-transfer and the inductive-resistive phenomena through the interaction with adsorbed OH-species to decrease the CO-poisoning. In this context, the poisoning effect was low considering the contribution of more Pd-oxide species in the Pd/HDA/C@air-ht catalyst with respect also with the material from commercial source. The superior electrocatalytic performance of Pd/HDA/C@air-ht makes it a promising candidate for anodic catalyst at direct methanol fuel cell electricity-generators.

#### Acknowledgments

The authors wish to acknowledge the financial support provided by CONACyT (project 157613, 247208). Instituto Politécnico Nacional (COFAA, BEIFI-IPN-20180430) and SNI-CONACyT. Dirección de Investigación-Universidad Iberoamericana (UIA) F132021 project. C. Juárez-Balderas from the Departamento de Estudios en Ingeniería para la Innovación (UIA) for the heat treatments and fruitful comments, R. Borja-Urby from the Centro de Nanociencias y Micro Nanotecnologías (CNMN) and 2015 CONACyT-SEP basic research project 257931 for HR-TEM/STEM-EELS analyses. This collaborative research was also conducted in the framework of the “French-Mexican International Laboratory (LIA) devoted to Molecular Chemistry and its applications in Materials and Catalysis funded by CNRS and CONACyT. LPA G-O thanks the financial support from CONACyT within Doctor Fellowship.

## References

- [1] Liu Q, Lin Y, Fan J, Lv D, Min Y, Wu T, Xu Q (2016) Well-dispersed palladium nanoparticles on three-dimensional hollow N-doped graphene frameworks for enhancement of methanol electro-oxidation. *Electrochem Commun* 73:75–79
- [2] Kakati N, Maiti J, Lee SH, Jee SH, Viswanathan B, Yoon YS (2014) Anode catalysts for direct methanol fuel cells in acidic media: Do we have any alternative for Pt or Pt-Ru?. *Chem Rev* 114:12397–12429
- [3] M Noroozifar, M Khorasani-Motlagh, MS Ekrami-Kakhki, R Khaleghian-Moghadam (2014) Electrochemical investigation of Pd nanoparticles and MWCNTs supported Pd nanoparticles-coated electrodes for alcohols (C1-C3) oxidation in fuel cells. *J Appl Electrochem* 44:233–243
- [4] Yin Z, Zheng H, Ma D, Bao X (2009) Porous palladium nanoflowers that have enhanced methanol electro-oxidation activity. *J Phys Chem C* 113:1001–1005
- [5] Kannan P, Maiyalagan T, Opallo M (2013) One-pot synthesis of chain-like palladium nanocubes and their enhanced electrocatalytic activity for fuel-cell applications. *Nano Energy* 2:677–687
- [6] Pan W, Zhang X, Ma H, Zhang J (2008) Electrochemical synthesis, voltammetric behavior, and electrocatalytic activity of Pd nanoparticles. *J Phys Chem C* 112:2456–2461
- [7] Ding K, Yang G, Wei S, Mavinakuli P, Guo Z (2010) Cyclic voltammetric preparation of palladium nanoparticles for ethanol oxidation reaction. *Ind Eng Chem Res* 49:11415–11420
- [8] Cookson J (2012) The preparation of palladium nanoparticles. *Platin Met Rev* 56:83–98
- [9] Erikson H, Sarapuu A, Solla-Gullón J, Tammeveski K (2016) Recent progress in oxygen reduction electrocatalysis on Pd-based catalysts. *J Electroanal Chem* 780:327–336
- [10] Ramirez E, Eradès L, Philippot K, Lecante P, Chaudret B (2007) Shape control of platinum nanoparticles. *Adv Funct Mater* 17:2219–2228
- [11] Flanagan KA, Sullivan JA, Müller-Bunz H (2007) Preparation and characterization of 4-dimethylaminopyridine-stabilized palladium nanoparticles. *Langmuir* 23:12508–12520
- [12] Li Z, Gao J, Xing X, Wu S, Shuang S, Dong C, Paa MC, Choi MMF (2010) Synthesis and characterization of n -alkylamine-stabilized palladium nanoparticles for electrochemical oxidation of methane. *J Phys Chem C* 114:723–733
- [13] Chen S, Huang K, Stearns JA (2000) Alkanethiolate-protected palladium nanoparticles. *Chem Mater* 12 (2000) 540–547.
- [14] Sadeghmoghadam E, Lam C, Choi D, Shon Y-S (2011) Synthesis and catalytic properties of alkanethiolate-capped Pd nanoparticles generated from sodium S-dodecylthiosulfate. *J Mater Chem* 21:307–312

- [15] Gupta D, Dutta D, Kumar M, Barman PB, Sarkar CK, Basu S, Hazra SK (2014) A low temperature hydrogen sensor based on palladium nanoparticles. *Sensors Actuators B Chem* 196:215–222
- [16] Yee CK, Jordan R, Ulman A, White H, King A, Rafailovich M, Sokolov J (1999) Novel one-phase synthesis of thiol-functionalized gold, palladium, and iridium nanoparticles using superhydride, *Langmuir* 15:3486–3491
- [17] Kim YG, Garcia-Martinez JC, Crooks RM (2005) Electrochemical properties of monolayer-protected Au and Pd nanoparticles extracted from within dendrimer templates. *Langmuir* 21:5485–5491
- [18] Cliffler DE, Zamborini FP, Gross SM, Murray RW (2000) Mercaptoammonium-monolayer-protected, water-soluble gold, silver, and palladium clusters. *Langmuir* 16:9699–9702
- [19] Niu W, Li ZY, Shi L, Liu X, Li H, Han S, Chen J, Xu G (2008) Seed-mediated growth of nearly monodisperse palladium nanocubes with controllable sizes. *Cryst Growth Des* 8:4440–4444
- [20] Erikson H, Sarapuu A, Tammeveski K, Solla-Gullón J, Feliu JM (2011) Enhanced electrocatalytic activity of cubic Pd nanoparticles towards the oxygen reduction reaction in acid media. *Electrochem Commun* 13:734–737
- [21] Grigoriev SA, Millet P, Fateev VN (2008) Evaluation of carbon-supported Pt and Pd nanoparticles for the hydrogen evolution reaction in PEM water electrolyzers. *J Power Sources* 177:281–285
- [22] Yamada M, Quiros I, Mizutani J, Kubo K, Nishihara H (2001) Preparation of palladium nanoparticles functionalized with biferrocene thiol derivatives and their electro-oxidative deposition. *Phys Chem Chem Phys* 3:3377–3381
- [23] Kim S-W, Park J, Jang Y, Chung Y, Hwang S, Hyeon T, Kim YW (2003) Synthesis of monodisperse palladium nanoparticles. *Nano Lett* 3:1289–1291
- [24] Mazumder V, Sun S (2009) Oleylamine-mediated synthesis of Pd nanoparticles for catalytic formic acid oxidation. *J Am Chem Soc* 131:4588–4589
- [25] Shi Y, Yin S, Ma Y, Lu D, Chen Y, Tang Y, Lu T (2014) Oleylamine-functionalized palladium nanoparticles with enhanced electrocatalytic activity for the oxygen reduction reaction. *J Power Sources* 246:356–360
- [26] Góral-Kurbiel M, Drelinkiewicz A, Kosydar R, Dembińska B, Kulesza PJ, Gurgul J (2014) Palladium content effect on the electrocatalytic activity of palladium-polypyrrole nanocomposite for cathodic reduction of oxygen. *Electrocatalysis* 5:23–40
- [27] Fu G, Jiang X, Tao L, Chen Y, Lin J, Zhou Y, Tang Y, Lu T (2013) Polyallylamine functionalized palladium icosahedra: One-pot water-based synthesis and their superior electrocatalytic activity and ethanol tolerant ability in alkaline media. *Langmuir* 29:4413–4420

- [28] Zhao S, Zhang H, House SD, Jin R, Yang JC, Jin R (2016) Ultrasmall palladium nanoclusters as effective catalyst for oxygen reduction reaction. *ChemElectroChem* 3:1–6
- [29] Naresh N, Wasim FGS, Ladewig BP, Neergat M (2013) Removal of surfactant and capping agent from Pd nanocubes (Pd-NCs) using tert-butylamine: its effect on electrochemical characteristics. *J Mater Chem A* 1:8553–8559
- [30] Nalajala N, Gooty Saleha WF, Ladewig BP, Neergat M (2014) Sodium borohydride treatment: a simple and effective process for the removal of stabilizer and capping agents from shape-controlled palladium nanoparticles. *Chem Commun* 50:9365–9368
- [31] Ramirez E, Jansat S, Philippot K, Lecante P, Gomez M, Masdeu-Bultó AM, Chaudret B (2004) Influence of organic ligands on the stabilization of palladium nanoparticles. *J Organomet Chem* 689:4601–4610
- [32] Jansat S, Gómez M, Philippot K, Muller G, Guiu E, Claver C, Castellón S, Chaudret B (2004) A case for enantioselective allylic alkylation catalyzed by palladium nanoparticles. *J Am Chem Soc* 126:1592–1593
- [33] Guerrero M, García-Antón J, Tristany M, Pons J, Ros J, Philippot K, Lecante P, Chaudret B (2010) Design of new N,O hybrid pyrazole derived ligands and their use as stabilizers for the synthesis of Pd nanoparticles. *Langmuir* 26:15532–15540
- [34] Siril PF, Lehoux A, Ramos L, Beaunier P, Remita H (2012) Facile synthesis of palladium nanowires by a soft templating method. *New J Chem* 36:2135–2139
- [35] Jose D, Jagirdar BR (2010) Synthesis and characterization of Pd(0), PdS, and Pd@PdO core-shell nanoparticles by solventless thermolysis of a Pd-thiolate cluster. *J Solid State Chem* 183:2059–2067
- [36] Cueva P, Hovden R, Mundy JA, Xin HL, Muller DA (2012) Data processing for atomic resolution electron energy loss spectroscopy. *Microsc Microanal* 18:667–675
- [37] Egerton RF (1996) *Electron Energy Loss Spectroscopy in the Electron Microscope* 2nd edn. Plenum, New York
- [38] Su PC, Chen HS, Chen TY, Liu CW, Lee CH, Lee JF, Chan TS, Wang KW (2013) Enhancement of electrochemical properties of Pd/C catalysts toward ethanol oxidation reaction in alkaline solution through Ni and Au alloying. *Int J Hydrogen Energy* 38:4474–4482
- [39] Xiong Y, Chen J, Wiley B, Xia Y, Yin Y, Li ZY (2005) Size-dependence of surface plasmon resonance and oxidation for Pd nanocubes synthesized via a seed etching process. *Nano Lett* 5:1237–1242

- [40] Jensen H, Pedersen JH, Jørgensen JE, Pedersen JS, Joensen KD, Iversen SB, Søgaard EG (2006) Determination of size distributions in nanosized powders by TEM, XRD, and SAXS. *J Exp Nanosci* 1:355–373
- [41] Dimitratos N, Lopez-Sanchez JA, Lennon D, Porta F, Prati L, Villa A (2006) Effect of particle size on monometallic and bimetallic (Au,Pd)/C on the liquid phase oxidation of glycerol. *Catal Letters* 108:147–153
- [42] Roddatis V, Kuznetsov VL, Butenko YV, Su DS, Schlögl R (2002) Transformation of diamond nanoparticles into carbon onions under electron irradiation. *Phys Chem Chem Phys* 4:1964–1967
- [43] Langenhors FT, Solozhenko VL (2002) ATEM-EELS study of new diamond-like phases in the B–C–N system. *Phys Chem Chem Phys* 4:5183–5188
- [44] Uppireddi K, Resto O, Weiner BR, Morell G (2008) Iron oxide nanoparticles employed as seeds for the induction of microcrystalline diamond synthesis. *Nanoscale Res Lett* 3:65–70
- [45] Waidmann S, Knupfer M, Fink J, Kleinsorge B, Robertson J (2001) Electronic structure studies of undoped and nitrogen-doped tetrahedral amorphous carbon using high-resolution electron energy-loss spectroscopy. *J Appl Phys* 89:3783–3792
- [46] Chen W, Zhang Y, Wei X (2015) Catalytic performances of PdNi/MWCNT for electrooxidations of methanol and ethanol in alkaline media. *Int J Hydrogen Energy* 40:1154–1162
- [47] Tura JM, Regull P, Victori L, de Castellar MD (1988) XPS and IR (ATR) analysis of Pd oxide films obtained by electrochemical methods. *Surf Interface Anal* 11:447–449
- [48] Zemlyanov D, Aszalos-Kiss B, Kleimenov E, Teschner D, Zafeiratos S, Hävecker M, Knop-Gericke A, Schlögl R, Gabasch H, Unterberger W, Hayek K, Klötzer B (2006) In situ XPS study of Pd(1 1 1) oxidation. Part 1: 2D oxide formation in  $10^{-3}$ mbar  $O_2$ . *Surf Sci* 600:983–994
- [49] Kim KS, Gossmann AF, Winograd N (1974) X-ray photoelectron spectroscopic studies of palladium oxides and the palladium-oxygen electrode. *Anal Chem* 46:197–200
- [50] Voogt EH, Mens JM, Gijzeman OLJ, Geus JW (1996) XPS analysis of palladium oxide layers and particles. *Surf Sci* 350:21–31
- [51] JLv Jing, Li S-S, Wang A-J, Mei L-P, Feng J-J, Chen J-R, Chen Z (2014) One-pot synthesis of monodisperse palladium-copper nanocrystals supported on reduced graphene oxide nanosheets with improved catalytic activity and methanol tolerance for oxygen reduction reaction. *J Power Sources* 269:104–110
- [52] Bastl Z (1995) X-Ray photoelectron spectroscopic studies of palladium dispersed on carbon surfaces modified by ion beams and plasmatic oxidation. *Collect Czech Chem Commun* 60:383–392

- [53] Moddeman WE, Bowling WC, Carter DC, Grove DR (1988) XPS Surface and bulk studies of heat-treated palladium in the presence of hydrogen at 150 °C. *Surf Interface Anal* 11:317–326
- [54] Evangelisti C, Panziera N, Pertici P, Vitulli G, Salvadori P, Battocchio C, Polzonetti G (2009) Palladium nanoparticles supported on polyvinylpyridine: Catalytic activity in Heck-type reactions and XPS structural studies. *J Catal* 262:287–293
- [55] Kibis LS, Stadnichenko AI, Koscheev SV, Zaikovskii VI, Boronin AI (2012) Highly oxidized palladium nanoparticles comprising Pd<sup>4+</sup> species: Spectroscopic and structural aspects, thermal stability, and reactivity. *J Phys Chem C* 116:19342–19348
- [56] Moulder JF, Stickle WF, Sobol PE, Bomben KD (1992) *Handbook of X-ray photoelectron spectroscopy*, Perkin-Elmer Corporation, Physical Electronics Division, Eden Prairie, Minnesota
- [57] Schmitz PJ, Otto K, de Vries JE (1992) An X-ray photoelectron spectroscopy investigation of palladium in automotive catalysts. Binding energies and reduction characteristics *Appl Catal A Gen* 92:59–72
- [58] Shafeev GA, Themlin JM, Bellard L, Marine W, Cros A (1996) Enhanced adherence of area-selective electroless metal plating on insulators. *J Vac Sci Technol A* 14:319–326.
- [59] Pillo T, Zimmermann R, Steiner P, Hübner S (1997) The electronic structure of PdO found by photoemission (UPS and XPS) and inverse photoemission (BIS). *J Phys Condens Matter* 9:3987–3999
- [60] Li DN, Wang AJ, Wei J, Zhang QL, Feng JJ (2018) Dendritic platinum-palladium/palladium core-shell nanocrystals/reduced graphene oxide: One-pot synthesis and excellent electrocatalytic performances. *J Colloid Interface Sci* 514:93–101
- [61] Kibis LS, Titkov AI, Stadnichenko AI, Koscheev SV, Boronin AI (2009) X-ray photoelectron spectroscopy study of Pd oxidation by RF discharge in oxygen. *Appl Surf Sci* 255:9248–9254
- [62] Wang F, Yu H, Tian Z, Xue H, Feng L (2018) Active sites contribution from nanostructured interface of palladium and cerium oxide with enhanced catalytic performance for alcohols oxidation in alkaline solution. *J Energy Chem* 27:395–403
- [63] Liu L, Lin X-X, Zou S-Y, Wang A-J, Chen J-R, Feng J-J (2016) One-pot wet-chemical synthesis of PtPd@Pt nanocrystals supported on reduced graphene oxide with highly electrocatalytic performance for ethylene glycol oxidation. *Electrochim Acta* 187:576–583
- [64] Légaré P, Finck F, Roche R, Maire G (1989) XPS investigation of the oxidation of the Al/Pd interface: The Al<sub>2</sub>O<sub>3</sub>/Pd interface. *Surf Sci* 217:167–178
- [65] Lee H, Shin M, Lee M, Hwang YJ (2015) Photo-oxidation activities on Pd-doped TiO<sub>2</sub> nanoparticles: critical PdO formation effect. *Appl Catal B Environ* 165:20–26

- [66] Bertolini JC, Delichere P, Khanra BC, Massardier J, Noupa C, Tardy B (1990) Electronic properties of supported Pd aggregates in relation with their reactivity for 1,3-butadiene hydrogenation. *Catal Letters* 6:215–224
- [67] Tressaud A, Khairoun S, Touhara H, Watanabe N (1986) X-Ray photoelectron spectroscopy of palladium fluorides. *Z Anorg Allg Chem* 540/541:291–299
- [68] Fleisch TH, Zajac GW, Schreiner JO, Mains GJ (1986) An XPS study of the UV photoreduction of transition and noble metal oxides. *Appl Surf Sci* 26:488–497
- [69] Boronin AI, Slavinskaya EM, Danilova IG, Gulyaev RV, Amosov YI, Kuznetsov PA, Polukhina IA, Koscheev SV, Zaikovskii VI, Noskov AS (2009) Investigation of palladium interaction with cerium oxide and its state in catalysts for low-temperature CO oxidation. *Catal Today* 144:201–211
- [70] Lupan O, Postica V, Hoppe M, Wolff N, Polonskyi O, Pauporté T, Viana B, Majérus O, Kienle L, Faupel F, Rainer A (2018) PdO/PdO<sub>2</sub> functionalized ZnO: Pd films for lower operating temperature H<sub>2</sub> gas sensing. *Nanoscale* 10:14107–14127
- [71] Guimarães AL, Dieguez LC, Schmal M (2003) Surface sites of Pd/CeO<sub>2</sub>/Al<sub>2</sub>O<sub>3</sub> catalysts in the partial oxidation of propane. *J Phys Chem B* 107:4311–4319
- [72] Peuckert M (1985) XPS study on surface and bulk palladium oxide, its thermal stability, and a comparison with other noble metal oxides. *J Phys Chem* 89:2481–2486
- [73] Bespalov I, Datler M, Buhr S, Drachsel W, Rupprechter G, Suchorski Y (2015) Initial stages of oxide formation on the Zr surface at low oxygen pressure: An in situ FIM and XPS study, *Ultramicroscopy*. 159:147–151
- [74] Jiang B, Song S, Wang J, Xie Y, Chu W, Li H, Xu H, Tian C, Fu H (2014) Nitrogen-doped graphene supported Pd@PdO core-shell clusters for C-C coupling reactions. *Nano Res* 7:1280–1290
- [75] Davi M, Keßler D, Slabon A (2016) Electrochemical oxidation of methanol and ethanol on two-dimensional self-assembled palladium nanocrystal arrays. *Thin Solid Films* 615:221–225
- [76] Grdeń M, Czerwiński A (2008) EQCM studies on Pd-Ni alloy oxidation in basic solution. *J Solid State Electrochem* 12:375–385
- [77] Liang ZX, Zhao TS, Xu JB, Zhu LD (2009) Mechanism study of the ethanol oxidation reaction on palladium in alkaline media. *Electrochim Acta* 54:2203–2208
- [78] Lukaszewski M, Soszko M, Czerwiński A (2016) Electrochemical methods of real surface area determination of noble metal electrodes - an overview. *Int J Electrochem Sci* 11:4442–4469
- [79] Correia AN, Mascaro LH, Machado SAS, Avaca LA (1997) Active surface area determination of Pd-Si alloys by H-adsorption. *Electrochim Acta* 42:493–495

- [80] Elezovic NR, Zabinski P, Ercius P, Wyrwal M, Radmilovic VR, Lačnjevac UC, Krstajic NV (2017) High surface area Pd nanocatalyst on core-shell tungsten based support as a beneficial catalyst for low temperature fuel cells application. *Electrochim Acta* 247:674–684
- [81] Soleimani-Lashkenari M, Rezaei S, Fallah J, Rostami H (2018) Electrocatalytic performance of Pd/PANI/TiO<sub>2</sub> nanocomposites for methanol electrooxidation in alkaline media. *Synth Met* 235:71–79
- [82] Ng JC, Tan CY, Ong BH, Matsuda A (2017) Effect of synthesis methods on methanol oxidation reaction on reduced graphene oxide supported palladium electrocatalysts. *Procedia Eng* 184:587–594.
- [83] Vidaković T, Christov M, Sundmacher K (2007) The use of CO stripping for in situ fuel cell catalyst characterization. *Electrochim Acta* 52:5606–5613
- [84] Zadick A, Dubau L, Demirci UB, Chatenet M (2016) Effects of Pd nanoparticle size and solution reducer strength on Pd/C electrocatalyst stability in alkaline electrolyte. *J Electrochem Soc* 163:F781–F787
- [85] Bäumer M, Libuda J, Neyman KM, Rösch N, Rupprechter G, Freund HJ (2007) Adsorption and reaction of methanol on supported palladium catalysts: microscopic-level studies from ultrahigh vacuum to ambient pressure conditions. *Phys Chem Chem Phys* 9:3541–3558
- [86] Chausse V, Regull P, Victori L (1987) Formation of a higher palladium oxide in the oxygen evolution potential range. *J Electroanal Chem* 238:115–128
- [87] Grdeń M, Łukaszewski M, Jerkiewicz G, Czerwiński A (2008) Electrochemical behavior of palladium electrode: Oxidation, electrodisolution and ionic adsorption. *Electrochim Acta* 53:7583–7598
- [88] Štrbac S, Maksić A, Rakočević Z (2018) Methanol oxidation on Ru/Pd(poly) in alkaline solution. *J Electroanal Chem* 823:161–170
- [89] Coutanceau C, Demarconnay L, Lamy C, Léger JM (2006) Development of electrocatalysts for solid alkaline fuel cell (SAFC). *J Power Sources* 156:14–19
- [90] Wang H, Sheng L, Zhao X, An K, Ou Z, Fang Y (2018) One-step synthesis of Pt-Pd catalyst nanoparticles supported on few-layer graphene for methanol oxidation. *Curr Appl Phys* 18:898–904